

# Magneto-elastic Effects in $\text{Tb}_3\text{Ga}_5\text{O}_{12}$

U. Löw,<sup>1</sup> S. Zherlitsyn,<sup>2</sup> K. Araki,<sup>3</sup> M. Akatsu,<sup>4</sup>  
Y. Nemoto,<sup>4</sup> T. Goto,<sup>4</sup> U. Zeitler,<sup>5</sup> and B. Lüthi<sup>6</sup>

<sup>1</sup>*Theoretische Physik II, Technische Universität Dortmund, 44227 Dortmund, Germany*

<sup>2</sup>*Hochfeld-Magnetlabor Dresden, Helmholtz-Zentrum  
Dresden-Rossendorf, D-01314 Dresden, Germany*

<sup>3</sup>*Institute for Solid State Physics, University of Tokyo, Kashiwa, Chiba 277-8581, Japan*

<sup>4</sup>*Graduate School of Science and Technology,  
Niigata University, Niigata 950-2181, Japan*

<sup>5</sup>*High Field Magnet Laboratory and Institute for Molecules and Materials,  
Radboud University Nijmegen, Toernooiveld 7,  
6525 ED Nijmegen, The Netherlands*

<sup>6</sup>*Physikalisches Institut, Johann Wolfgang Goethe  
Universität Frankfurt, D-60438 Frankfurt (M), Germany*

(Dated: September 17, 2018)

## Abstract

We report new results for the elastic constants studied in Faraday and Cotton-Mouton geometry in  $\text{Tb}_3\text{Ga}_5\text{O}_{12}$  (TGG), a frustrated magnetic substance with the strong spin-phonon interaction and remarkable crystal-electric-field (CEF) effects. We analyze the data in the framework of CEF theory taking into account the individual surroundings of the six inequivalent  $\text{Tb}^{3+}$ -ion positions. This theory describes both, elastic constants in the magnetic field and as a function of temperature. Moreover we present sound-attenuation data for the acoustic Cotton-Mouton effect in TGG.

72.55.+s, 73.50.Rb, 62.65+k

PACS numbers:

## I. INTRODUCTION

$\text{Tb}_3\text{Ga}_5\text{O}_{12}$  (TGG) is a dielectric material with the cubic garnet structure. The garnet structure materials show a wide spectrum of physical properties: interesting magnetic properties are found in the ferrimagnetic YIG or the rare earth series RIG (with R a heavy rare earth element) or the special DAG (dysprosium aluminum garnet), but also Laser properties such as in RAIG are found. For an early review see Ref. [1].

The garnet material TGG, described here, was in the center of interest in recent years. Unconventional experiments were carried out with this substance, e.g. the so-called phonon Hall effect [2, 3] and the acoustic Faraday effect [4, 5]. Most recently a detailed study of magnetic properties has been performed including ESR experiments to analyze the crystal electric field (CEF) of the  $\text{Tb}^{3+}$ -ion [6]. Using elastic neutron scattering, an antiferromagnetic (AFM) transition was observed at  $T_N = 0.35$  K, which was much lower than the Curie-Weiss temperature,  $\Theta_{CW} \sim 8.61$  K, evidencing very high level of magnetic frustrations [7].

In the present paper we proceed with the description of the CEF developed in our earlier work [6] and generalize it to include strain phenomena such as the temperature and magnetic field dependence of the elastic constants. Note, that only a simple cubic CEF model was used before to describe the temperature dependence of elastic constants in TGG [8]. Furthermore, we show magneto-acoustic birefringence data and fits discussing new experimental results obtained both in the Faraday and Cotton-Mouton geometry.

The ultrasound experiments have been performed on a TGG single crystal oriented for propagating the sound wave with wave vector  $\vec{k}$  along the [100] direction. The same sample as in Ref. [5] has been used in these experiments. The sample length along the direction of the sound-wave propagation was  $L_0 = 4.005$  mm. The sound velocity and attenuation have been measured with a setup as described at great length in Ref. [12].  $\text{LiNbO}_3$  transducers have been used in these experiments. Fields up to 33 T have been provided by a resistive magnet at the High Field Magnet Laboratory at Radboud University Nijmegen. The magnet has been equipped with a  $^3\text{He}$  cryostat.

The paper is organized as follows. In the next chapter we discuss the  $\text{Tb}_3\text{Ga}_5\text{O}_{12}$  (TGG) CEF model and include the quadrupolar operators which are necessary to describe the magneto-elastic interaction. Then we show and discuss the temperature and magnetic field

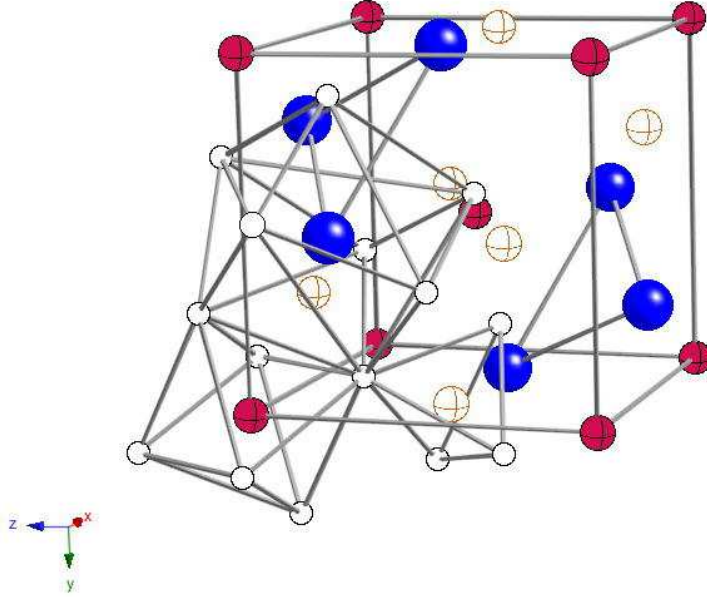


FIG. 1: (Color on line) Crystal-structure of TGG: Tb-ions blue (large filled spheres), Ga-ions red (small filled spheres) and O-ions white (empty spheres).

dependence of the elastic constants. We treat specifically the high field behaviour of the  $c_{44}$  mode which was measured in the acoustic Faraday and Cotton-Mouton geometry. The effect of the low lying quasi doublet on the elastic modes will be investigated because of its relevance for the phonon Hall effect. The magneto-elastic coupling constants gained from these discussions can be used for the interpretation of the phonon Hall effect. In addition to the Faraday effect [4, 5] we present also sound-attenuation data for the Cotton-Mouton-Voigt effect.

## II. THE CRYSTAL ELECTRIC FIELD IN TGG

In Fig. 1 the structure of TGG is shown. The Ga ions are located on cubic corner points whereas the Tb<sup>3+</sup> ions form corner sharing triangles. The Tb<sup>3+</sup> ions have eight  $4f$ -electrons leading with Hund's rule to  $S = 3$ ,  $L = 3$  and  $J = 6$ . Each Tb<sup>3+</sup> ion has the same orthorhombic  $D_2$  symmetry in its own local coordinate system and can be described by the

crystal field Hamiltonian, introduced by Guillot et al. [9]:

$$\begin{aligned}
 H = & b_{20}\mathcal{O}_{20} + b_{22}\mathcal{O}_{22} + b_{40}\mathcal{O}_{40} + b_{42}\mathcal{O}_{42} + b_{44}\mathcal{O}_{44} \\
 & + b_{60}\mathcal{O}_{60} + b_{62}\mathcal{O}_{62} + b_{64}\mathcal{O}_{64} + b_{66}\mathcal{O}_{66} + g\mu_B\vec{B}\vec{J}.
 \end{aligned}
 \tag{1}$$

Here  $\vec{B}$  is the magnetic field in the local coordinate system of a  $\text{Tb}^{3+}$  ion. The  $\mathcal{O}_{ij}$  are the Stevens operators [10], and the  $b_{ij}$  are the crystal field parameters [9], [11]. The table of the crystal field parameters and the explicit form of the Stevens operators are given in the Appendix (eqs. 12-20).

In this paper we use the Hamiltonian with orthorhombic point symmetry given by eq. 1 and take into account the six inequivalent ion positions in the unit cell [13] to calculate the elastic constants of TGG. We found it most convenient to rotate the Hamiltonians of eq. 1 from the six local coordinate systems which we denote by  $l_i$  with  $i = 1, \dots, 6$  to the laboratory system and then perform all the calculations in the laboratory system. In particular for the magneto-elastic coupling this is the best way to proceed, because thus there is no need to transform the calculated elastic constants back to the laboratory system. For these calculations we used the rotation matrices  $R(\alpha_i, \beta_i, \gamma_i)$  where  $\alpha_i, \beta_i, \gamma_i$  are the Euler angles. Following the notation of Edmonds [14] the Euler angles of the rotations from the local systems  $l_i$  to the laboratory system can be easily obtained and are explicitly given in the Appendix (eq. 21).

The rotated Hamiltonians, calculated by use of Mathematica, have in general complex coefficients. In contrast to the original Hamiltonian eq. 1 also operators of the type  $\mathcal{O}_{l,+j}$  and  $\mathcal{O}_{l,-j}$  appear. For these more general cases for which the operators are not listed in [10] we use the form of the operators given by P.A. Lindgård, O. Danielsen [17]. As an example, in the Appendix (eq. 23) we list the coefficients  $b_{i\pm j}^1$  of the resulting Hamiltonian  $\mathcal{H}^1$  obtained by rotating eq.1 with  $\vec{B} = 0$  from  $l_1$  to the laboratory system.

In [6] we calculated the energy levels of the different ions in a magnetic field parallel to the cubic  $[110]_c$ ,  $[100]_c$  and  $[111]_c$  direction. Here in Fig. 2 we show the energy levels for the convenience again.

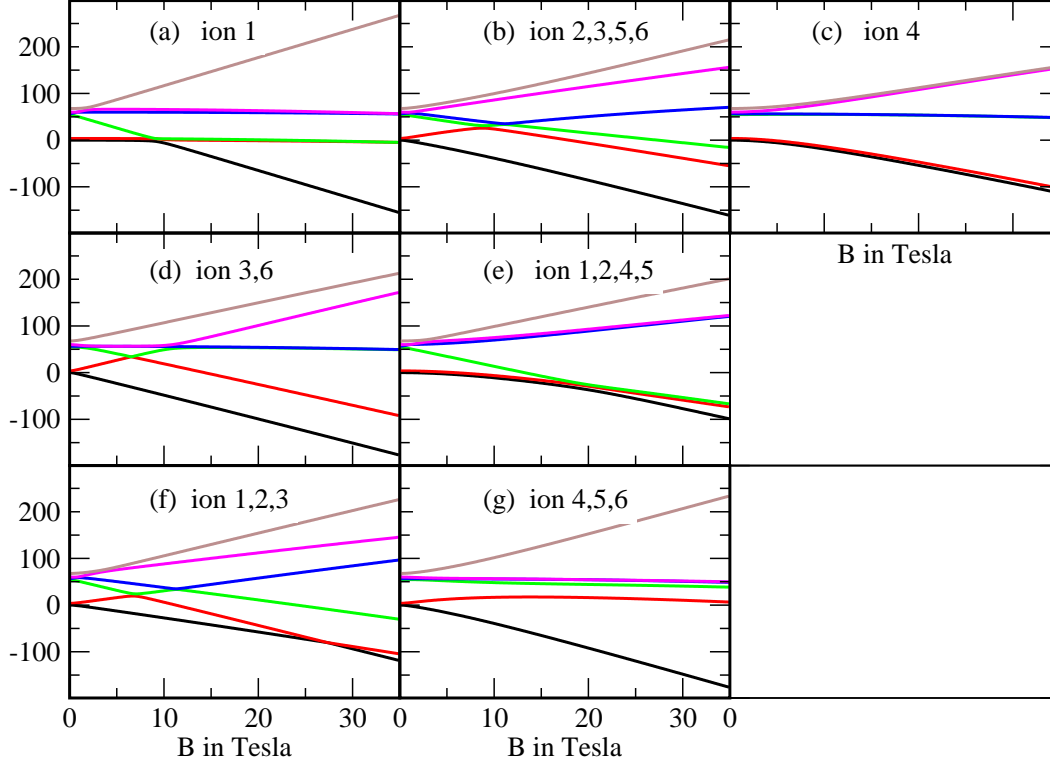


FIG. 2: (Color on line) Panels a,b,c show the six lowest energy levels for field in  $[110]_c$  direction, panels d,e are the corresponding levels for field in  $[100]_c$  direction, and panels f,g for field in  $[111]_c$  direction. The corresponding ions are marked in the figure, the energies are in Kelvin and the magnetic field is in Tesla.

### III. THE MAGNETO-ELASTIC COUPLING

Next we turn our attention to the elastic constants. For an overview of various magneto-elastic couplings see Ref. [12]. We note that, the temperature dependence of the elastic constants has been previously described in a cubic approximation [8]. Here we refine the description by incorporating the local surroundings of the ions in the framework described in chapter II. Using this approach we investigate longitudinal and transverse elastic constants  $c_{11}$ ,  $c' = (c_{11} - c_{12})/2$ ,  $c_{44}$ , the bulk modulus  $c_B$ , and their couplings to the corresponding quadrupole operators.

Profiting from the rotation of the local Hamiltonians we have performed, it suffices now to consider the cubic symmetry strains in the laboratory system: the volume strain  $e_V = e_{xx} + e_{yy} + e_{zz}$  with  $c_B = (c_{11} + 2c_{12})/3$ , the  $\Gamma_3$ -strain  $e_2 = (e_{xx} - e_{yy})/\sqrt{2}$  with  $c' = (c_{11} - c_{12})/2$ ,

and the  $\Gamma_5$  shear strain  $e_{xy}$ .

The magneto-elastic Hamiltonian in the laboratory coordinate system reads

$$H_{me} = g(\Gamma_3)e_2\mathcal{O}_{22} + g(\Gamma_5)e_{xy}\mathcal{O}_{xy}, \quad (2)$$

where  $g(\Gamma_3)$  and  $g(\Gamma_5)$  are coupling constants determined from the experiment and  $\mathcal{O}_{xy} = \frac{1}{2}(J_xJ_y + J_yJ_x)$  and  $\mathcal{O}_{22} = (J_x^2 - J_y^2)$  are quadrupole operators. Here we calculate using magneto-elastic Hamiltonian  $H_{me}$  of eq. 2 the elastic constants  $(c_{11} - c_{12})/2$  and  $c_{44}$ . The case of  $c_B$  will be mentioned later.

Since in an ultrasonic wave the strains are small one can use perturbation theory to calculate the strain dependence of the CEF energy levels  $E_n(\epsilon_\Gamma)$  and of the free energy (see ref. [12]). The second order terms in this expansion are the the strain susceptibilities  $\chi(T)$  defined (in analogy to the magnetic susceptibility) as the response of a structural order parameter  $\langle \mathcal{O} \rangle$  to an applied strain  $e$ :

$$\begin{aligned} \chi(T) = \frac{1}{Ng^2}\Delta c = \frac{1}{Ng^2} \left. \frac{\partial^2 F}{\partial e^2} \right|_{e=0} &= \frac{1}{Z^2} \frac{1}{k_B T} \left( \sum_n \langle n | \mathcal{O} | n \rangle \exp\left(\frac{-E_n}{k_B T}\right) \right)^2 \\ &- \frac{1}{Z} \frac{1}{k_B T} \sum_n |\langle n | \mathcal{O} | n \rangle|^2 \exp\left(\frac{-E_n}{k_B T}\right) \\ &+ \frac{2}{Z} \sum_{n \neq m} \frac{|\langle n | \mathcal{O} | m \rangle|^2}{E_n - E_m} \exp\left(\frac{-E_n}{k_B T}\right). \end{aligned} \quad (3)$$

Here  $|n\rangle$  and  $E_n$  with  $n = 1, \dots, 13$  are the eigenstates and eigenvalues of the Hamiltonians  $\mathcal{H}^i$  obtained from eq. 1 by the above described rotations to the laboratory system and  $F$  and  $Z$  are the free energy and partition sum. Also in analogy to the magnetic susceptibility the first two contributions to  $\chi(T)$  are referred to as Curie terms, the last term as Van Vleck term. In general the Curie terms depend strongly on the temperature and the Van Vleck term has a relatively weak temperature dependence.

Using the magnetoelastic Hamiltonian eq. 2 the change in the elastic constants and the corresponding strain susceptibilities  $\chi$  are given by:

$$\Delta c' = Ng^2(\Gamma_3) \frac{\partial \langle \mathcal{O}_{22} \rangle}{\partial e_2} = Ng^2(\Gamma_3)\chi(\Gamma_3) \quad (4)$$

and

$$\Delta c_{44} = Ng^2(\Gamma_5) \frac{\partial \langle \mathcal{O}_{xy} \rangle}{\partial e_{xy}} = Ng^2(\Gamma_5)\chi(\Gamma_5). \quad (5)$$

The strain susceptibilities are calculated for the six ions separately. The results are shown in Fig. 3. As can be seen from Fig. 3a there are two distinct curves contributing to  $\Delta c'$ , one

showing a broad minimum at about 30 K and distinct anomalies below 10 K and a second one which varies little with temperature above 25 K. We discuss the anomalies below 10 K in more detail in section IV. As shown in Fig. 3b there are also two type of curves contributing to  $\Delta c_{44}$  with minima at 10 K and 28 K. It may be worth noting that calculating  $c_{55}$  or  $c_{66}$  explicitly instead of  $c_{44}$  gives the same results as shown in Fig. 3 but with the role of the ions interchanged. The same interchanging of ions is encountered when considering  $(c_{33} - c_{13})/2$  instead of  $c'$ . This naturally reflects the cubic symmetry of the unit cell.

We fitted the curves to the experimental data shown in Fig. 4 averaging over the contributions of the six different ions of Fig. 3. Since the two ions number 2, 5 and the four ions 1,3,4,6 give identical results for the elastic modes  $c'$  and  $c_{44}$  for brevity we henceforward denote the strain susceptibilities and the magneto-elastic coupling constants with  $\chi_2$  and  $\chi_4$  and  $g_2$  and  $g_4$  respectively, using the multiplicity 2 and 4 as index.

Therefore we get

$$c' = c'_0 + \frac{N}{3} [2(g_4(\Gamma_3))^2 \chi_4(\Gamma_3) + (g_2(\Gamma_3))^2 \chi_2(\Gamma_3)] \quad (6)$$

$$c_{44} = (c_{44})_0 + \frac{N}{3} [2(g_4(\Gamma_5))^2 \chi_4(\Gamma_5) + (g_2(\Gamma_5))^2 \chi_2(\Gamma_5)]. \quad (7)$$

For the background we usually take the Varshny formula [16]. For the low temperature region in which we are mostly interested,  $c_0$  is almost constant.

The temperature dependence of the elastic constants  $c'$ ,  $c_{44}$ ,  $c_{11}$ , and  $c_B$  are given in Fig. 4. The first three propagating modes were measured directly and the non-propagating bulk modulus  $c_B$  is calculated using the formula

$$c_B = (c_{11} + 2c_{12})/3 = c_{11} - \frac{4}{3}c' \quad (8)$$

All three propagating modes can be described quantitatively using eqs. 6,7 and the corresponding strain susceptibilities of Fig. 3. For the fit of the longitudinal  $c_{11}$  mode we took the bulk modulus from eq. 8 and the calculated strain susceptibility for  $c'$  with the same magneto-elastic coupling constants  $g_{2,4}(\Gamma_3)$ . Especially the pronounced minimum at 30 K is given exactly with the calculated strain susceptibility for  $c_{44}$ . This mode is fitted particularly well.

	$g_2(\Gamma_5)$	$g_4(\Gamma_5)$	$g_2(\Gamma_3)$	$g_4(\Gamma_3)$	$g_F$	$g_{CM}$	$c_0(T=0)$
$c_{44}(\Gamma_5)$	193 K	98 K			81 K	55 K	$9.74 \cdot 10^{10}$
$c'(\Gamma_3) = (c_{11} - c_{12})/2$			0 K	114 K			$9.71 \cdot 10^{10}$
$c_{11}$			0 K	114 K			

TABLE I: Magneto-elastic coupling constants,  $g_i$ , and background elastic constants,  $c_0$ , in  $J/m^3$

The fits for  $c'$  and  $c_{11}$  are less satisfactory. The main reason is that the calculated minimum of  $\chi_4(\Gamma_3)$  is at 30 K like  $\chi_2(\Gamma_5)$  but experimentally the minima of  $c'$  and  $c_{11}$  are at 40 K. In addition  $\chi_2(\Gamma_3)$  has little structure and is much smaller than  $\chi_4(\Gamma_3)$ . Avoiding unrealistic large  $g_2(\Gamma_3)$  for the high temperature fit, for low temperatures a good fit results in a neglect of  $g_2$ . The fits for  $c'$  and  $c_{11}$  are therefore very good for  $T < 10$  K (see Fig. 5) but give only the salient features for higher temperatures (Fig. 4).

We suspect that higher order magneto-elastic couplings (hexadecapole moment-strain coupling) had to be considered for these modes. Such higher order couplings were introduced for a number of rare-earth compounds like PrSb, PrPb<sub>3</sub>, PrNi<sub>5</sub> [12]. The magneto-elastic coupling constants  $g_2$  and  $g_4$  used for the fit of the  $c'$ ,  $c_{11}$  and  $c_{44}$  modes are given in Table I.

The temperature dependence of the bulk modulus  $c_B$  shown also in Fig. 4 is anomalous. Below 100 K it decreases continuously. This means that  $c_B$  is also affected by the crystal field. Since  $e_V$  and  $c_B$  have  $\Gamma_1$ -symmetry this mode couples directly to the CEF Hamiltonian. Therefore we can write

$$H_{me}(c_B) = G_4 e_V (\mathcal{O}_{40} + 5\mathcal{O}_{44}) + G_6 e_V (\mathcal{O}_{60} - 21\mathcal{O}_{66}) \quad (9)$$

$G_4$   $G_6$  are coupling constants which can be determined by fitting the strain susceptibility deduced from eq. 9, to the  $c_B(T)$  curve of Fig. 4. This will be done together with the higher order susceptibility fits for  $c'$  and  $c_{11}$  in later work.



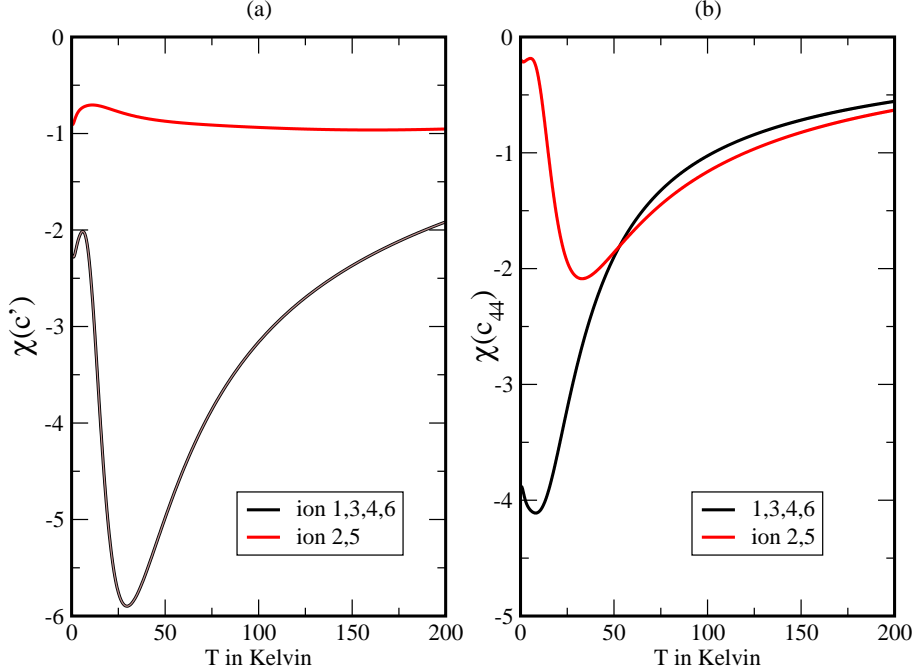


FIG. 3: (Color on line) Contributions to  $\chi(c')$  (left panel) and contributions to  $\chi(c_{44})$  (right panel) from the ions  $l_i$  for  $i = 1, \dots, 6$ .

#### IV. ELASTICITY DUE TO THE GROUND-STATE QUASI-DOUBLET AND THE RESONANT SPIN-PHONON EFFECTS

As seen in the temperature dependence of the various elastic constants in Fig. 4 there are, apart from the strong anomalies around 30 K, also weaker extrema for  $T < 4$  K. As demonstrated above these structures are well reproduced by the calculation (see Fig. 5). Inset of Fig. 5 shows a change of the slope in the  $c_{44}$  at the AFM ordering [7]. Note, that it is a rather unusual feature. One might more likely expect an anomaly at  $T_N$  in the acoustic properties of a longitudinal mode. In any case the small effect at  $T_N$  on  $c_{44}$  shows that the antiferromagnetic ordering has a negligible effect on  $c_{44}(T, B)$  displayed in the Figs. 8, 9, 10.

In the following we demonstrate that the low-temperature anomalies are mainly due to the quadrupolar couplings within the lowest states alone. For this the strain susceptibilities were calculated using a reduced ensemble of the lowest two and the lowest three states. The results are shown in Fig. 6. Comparing with Fig. 3 one sees that the low-temperature anomalies, similar to the ones shown in Figs. 4,5 can be found also in the calculation within the reduced ensemble. The strong minimum at 30 K is present only with three and higher

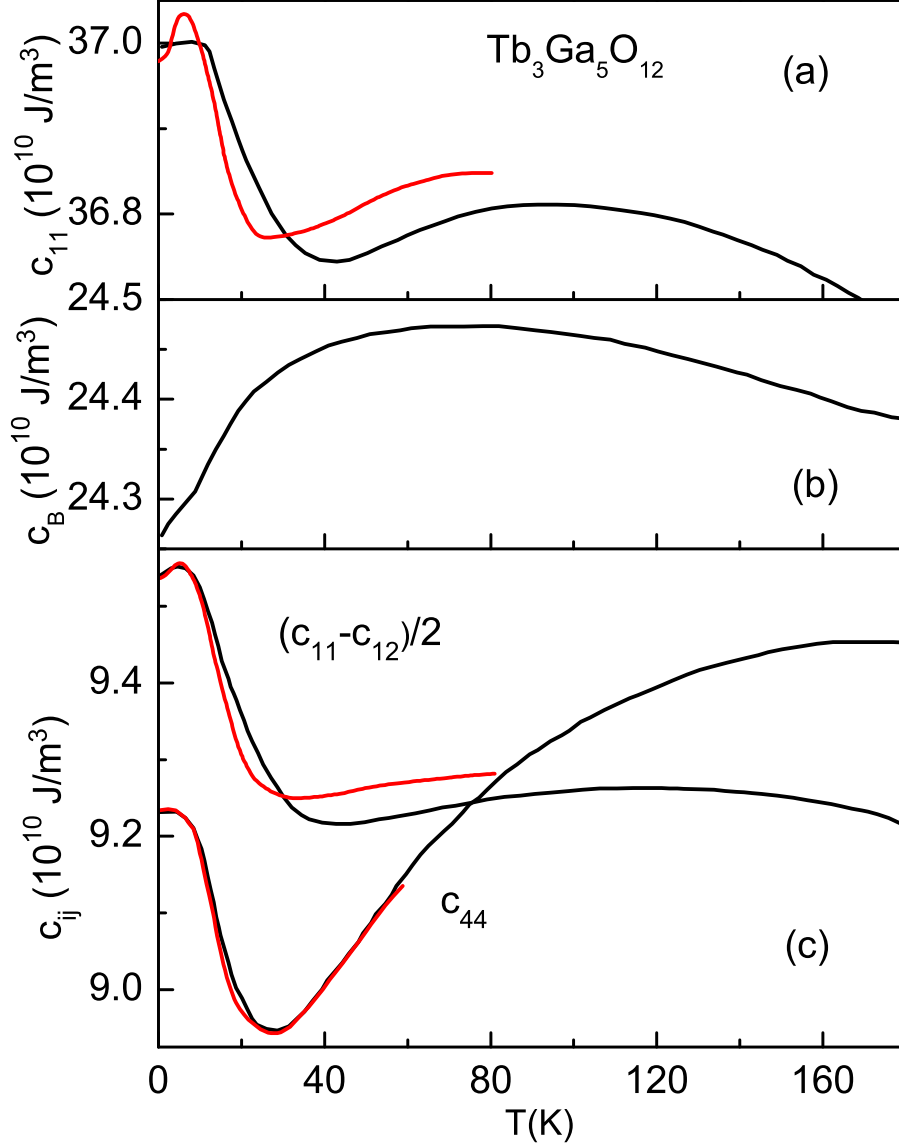


FIG. 4: (Color on line) Temperature dependence of the elastic constants  $c_{11}$ ,  $c_B$ ,  $c' = (c_{11} - c_{12})/2$ , and  $c_{44}$ . Experiment (black) and calculation (red). For the fit parameters and the background see Table I.

states included.

One should note, however, that the overall height of the strain susceptibility cannot be accounted for by using the lowest states alone, since matrix elements between the intermediate states substantially contribute to the strain susceptibilities also close to zero temperature. This is mainly due to the van Vleck contribution to the susceptibility. The partition function at low temperatures is, of course, well described by the lowest states alone.

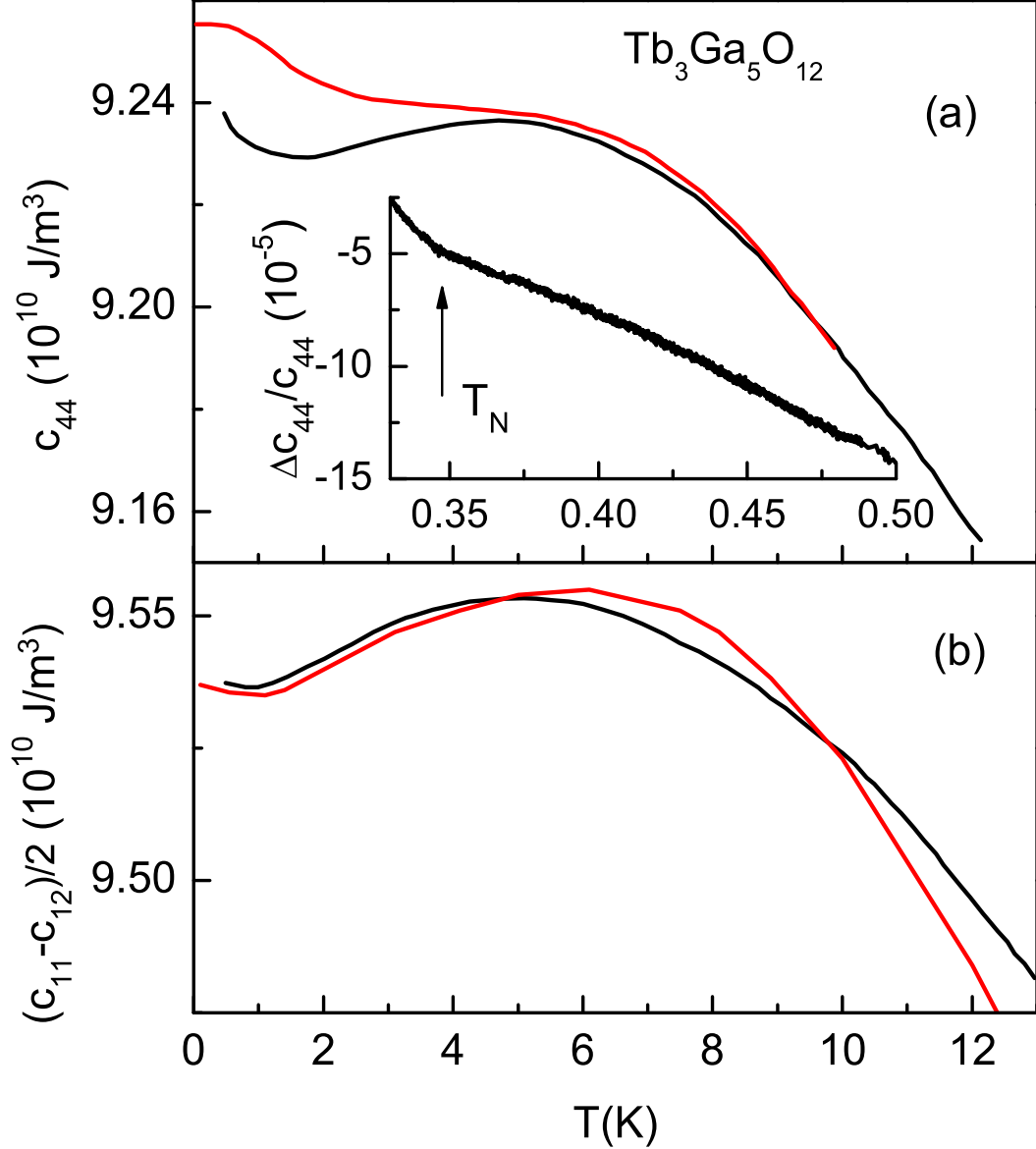


FIG. 5: (Color on line) Low temperature behaviour of the elastic constants. Experiment (black) and calculation (red). Inset shows a relative change of the elastic constant,  $c_{44}$ , below 0.5 K, in the vicinity of the AFM ordering.

The zero field splitting ( $B = 0$ ) of the quasi doublet (0,1) is 3.7 K as discussed in section II and Ref. [6]. This splitting is too large for a study of resonant phonon effects with coherent sound waves. The splitting corresponds to microwave phonons of 77 GHz. However in a thermal conductivity experiment this splitting was observed as a minimum at 0.52 K (see Ref. [19]). It was interpreted as a resonant phonon scattering process for a two-level system.

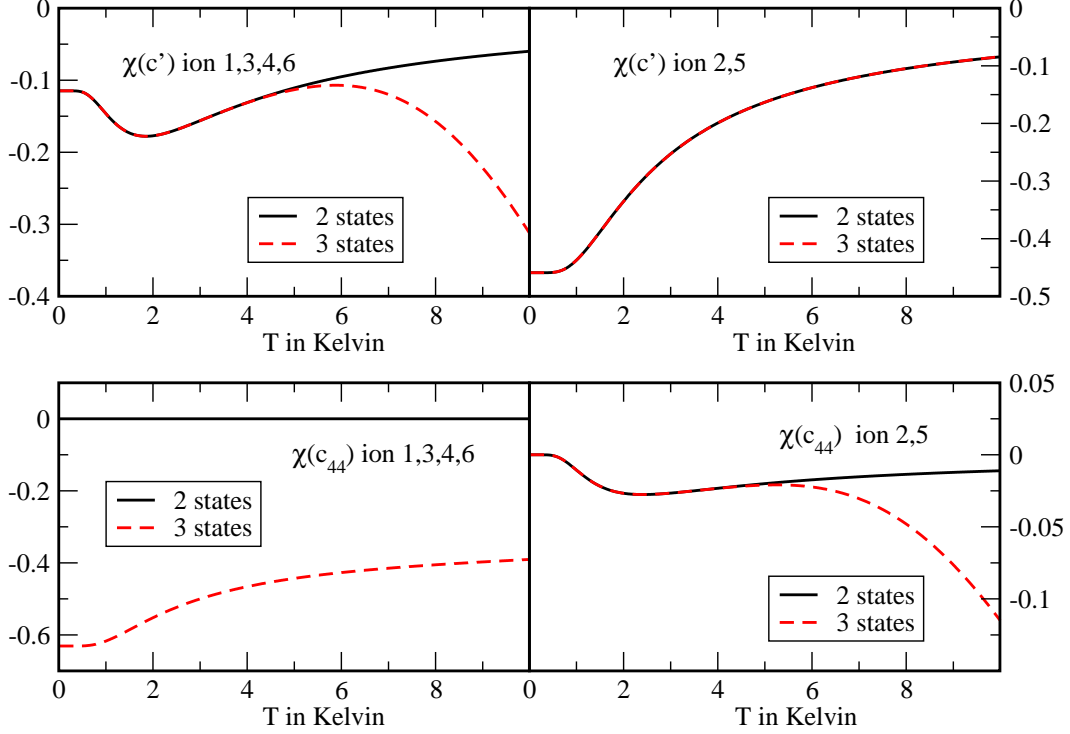


FIG. 6: (Color on line) Contributions of the lowest lying states to  $c' = (c_{11} - c_{12})/2$  and  $c_{44}$ .

Magnetic fields close the gap of the quasi doublet only with the additional energy level 3 for  $B = 9$  T ( $[110]_c$ -direction) and at  $B = 19$  T ( $[100]_c$ -direction) as shown in Fig. 2 and observed in ESR and magnetization experiments [6, 9]. Therefore sound attenuation experiments in magnetic fields in TGG do not provide ideal conditions for studying resonant spin-phonon interaction for a two-level system. Likewise the theory of the phonon-Hall effect in TGG should not treat only the quasi doublet but should take at least the lowest three states into account. In thermal conductivity the resonant interaction leads to strong thermal resistance [19].

## V. ELASTIC CONSTANTS IN MAGNETIC FIELD

We investigate elastic constants in magnetic fields for different geometries. One is the so-called Faraday geometry, another one the Cotton-Mouton-Voigt geometry. We use the same formalism to calculate the strain susceptibilities in the presence of a magnetic field. Now there are two independent directions given by the direction of the sound wave and of the magnetic field.

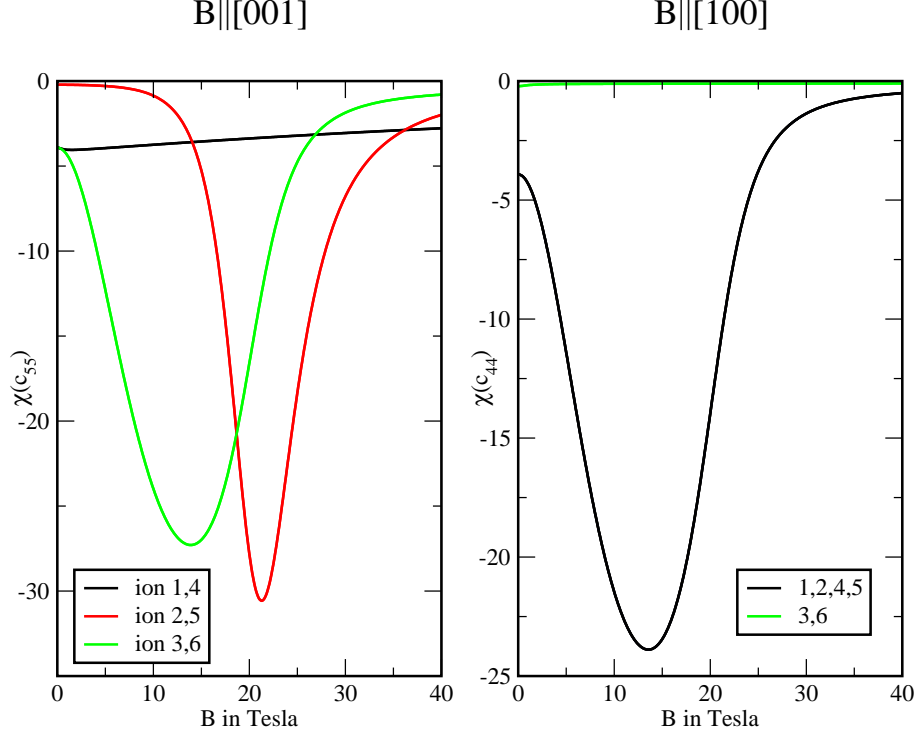


FIG. 7: (Color on line) Contributions to  $\chi(c_{55})$  for field in  $[001]_c$  direction (Faraday geometry) and contributions to  $\chi(c_{44})$  for field in  $[100]_c$  direction (CM geometry) from the ions  $l_i$  for  $i = 1, \dots, 6$ .

### A. Faraday geometry

This geometry was already discussed qualitatively in Ref. [5]. In Fig. 7 we give the calculated strain susceptibility for  $c_{44}$  with  $k||B||[001], u||[100]$  involving all 6 ions. The strain susceptibilities  $\chi(c_{55})$  in this case are degenerate for the three pairs (1,4), (2,5) and (3,6). If we assume the same magneto-elastic coupling constant for the three pairs we get the averaged susceptibility  $\chi_{av}$ , shown in Fig. 8. This  $\chi_{av}$  has the same form as the experimentally observed one also shown in Fig. 8. Therefore we take this  $\chi_{av}$  to fit the experiment using the formula

$$\Delta c_{44} = -g_F^2 N \chi_{av} \quad (10)$$

This gives a magneto-elastic coupling constant  $g_F = 80.6$  K. Note that eq. 10 gives the minimum exactly at the same field of 20.3 T as the experiment. The deviation at higher fields may be due to the averaging over the three pairs of ions. It could also be due to the

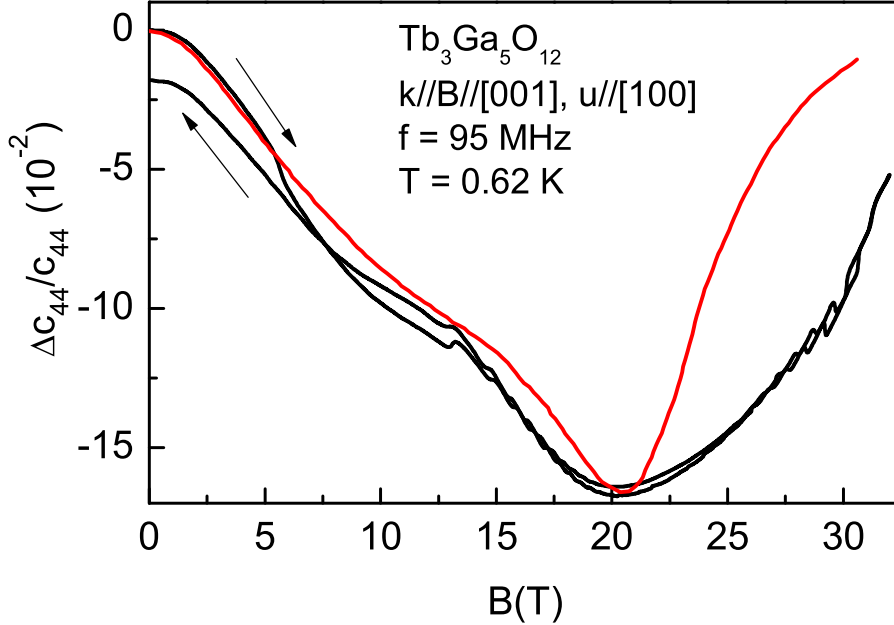


FIG. 8: (Color on line) Faraday configuration: Magnetic field dependence of the elastic constant,  $c_{44}$ , experiment (black, field sweeps up and down are shown) and calculation (red).

magneto-caloric effect, as calculated in Ref. [5].

### B. Cotton-Mouton geometry

Here we measured the elastic constant  $c_{44}$  for  $k||[001]$ ,  $u||[010]$  and  $B||[100]$ . The experimental result is shown in Fig. 9 for  $T = 1.34$  K and frequency of 340.7 MHz. The hysteresis for field increase and decrease is probably due to some heating effect, so the increasing one is closer to the given temperature. The calculated strain susceptibility  $\chi(c_{44})$  is also shown in Fig. 9. In this geometry four ions give identical results (1,2,4,5) whereas the remaining two (3,6) provide a negligibly small contribution. Therefore we obtain one coupling constant  $g_{CM}$  with an additional factor 4/6 for the strain susceptibility (see Fig.7).

In the case of the Cotton-Mouton geometry the minima of measured and calculated curves differ slightly. The measured minimum is at 11 T and the calculated one at 13.6 T. Since the form of the curves are very similar they are just shifted by 2 T from each other. The magneto-elastic coupling constant from the fit gives  $g_{CM} = 55.2$  K.

The important point is that in the Faraday geometry the minimum of the  $c_{44}$ -mode versus

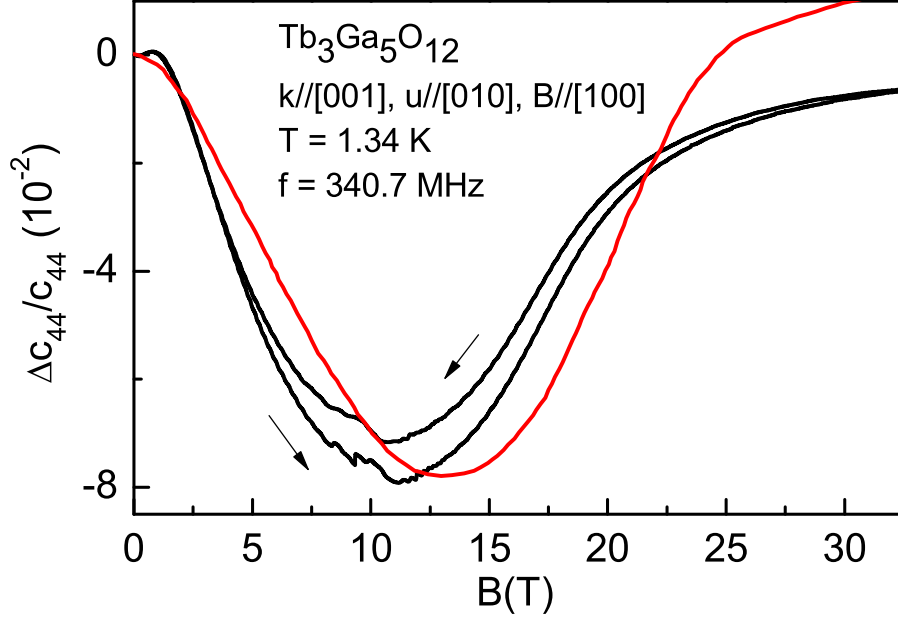


FIG. 9: (Color on line) Voigt configuration: Magnetic field dependence of the elastic constant,  $c_{44}$ , experiment (black, field sweeps up and down are shown) and calculation (red).

field is at 20.3 T in excellent agreement with our calculation, for the CM-geometry it is at a much lower field of 10 - 13 T in agreement with our calculation too. This gives strong support for the CEF scheme proposed in Ref [9] and also used for magnetic and ESR investigation in Ref. [6]. The minimum for the Faraday geometry is due to the crossover of the lowest two energy levels at 20 T as seen in Fig. 2. The broad minimum in the CM geometry is at a lower field because these ions experience a smaller field as seen from the calculated strain susceptibilities of Fig. 9.

Unfortunately we do not have results for the other Cotton-Mouton geometry:  $k||[001]$ ,  $u||B||[100]$ . This would have allowed us to investigate the influence of asymmetric strain contributions, the so-called rotationally invariant magneto-elastic contribution [12].

### C. Coupling constants discussion

In Table 1 we list the various magneto-elastic coupling constants from the temperature dependence and from the magnetic field dependence of the elastic constants. For the  $c_{44}$  mode which was investigated as a function of temperature and magnetic field we find the coupling constants all in the range from 50 to 200 K. Of course, the various  $g(\Gamma_5)$  have not

to be exactly the same, since the local coordinate systems differ with respect to the magnetic field direction. For the  $c'$  mode the negligible coupling constant,  $g_2$ , and the sizable value for  $g_4$  describe the low temperature properties quite well as seen in Fig. 5. The slight disagreements for higher temperatures are due to the different minima positions observed experimentally (40 K) and calculated (30 K). Possible further reasons for the disagreement were given in chapter III.

In this paper we investigated magneto-elastic couplings with single ion effects. We neglected two ion effects like e.g. a direct quadrupole-quadrupole interaction (see ref.[12] section 5.3) for the following reasons: For  $c'(T)$  such 2-ion effects do not improve the fit and for  $c_{44}(T)$  the fit is excellent without this additional coupling. For  $c_{44}(B)$  the inclusion of two ion effects is rather difficult because of the strong field dependence of the strain susceptibility of the 6 different ions (Fig.7). One had to introduce at least 2 - 3 more coupling constants which makes a fit meaningless.

## VI. ACOUSTIC COTTON-MOUTON EFFECT IN TGG

In previous papers [4, 5] we have studied the acoustic Faraday effect in TGG. Here we investigate the Cotton-Mouton-Voigt effect in this material. In the Faraday effect  $B \parallel \vec{k}$  which leads to a rotation of the polarization direction.

In the Cotton-Mouton effect  $B \perp \vec{k}$  which leads to birefringence. The velocities for  $B \parallel \vec{u}$  and  $B \perp \vec{u}$  are different so we encounter a phase change  $\frac{\Phi(B)}{L}$  for  $k \parallel [001], B \parallel [100], u \parallel [110]$  (see Ref. [12]) given by

$$\frac{\Phi(B)}{L} = \omega \left( \frac{1}{v_{100}} - \frac{1}{v_{010}} \right). \quad (11)$$

A typical example of the amplitude modulation of a given ultrasonic echo as a function of magnetic field is exhibited in Fig. 10b.

A linearly polarized wave with  $u \parallel [110]$  changes in the field to elliptically polarized and after a phase change of  $\pi/2$  to circularly polarized, followed by elliptical polarization and finally linearly polarization orthogonal to the original linearly polarization  $u \parallel [1\bar{1}0]$ . The phase difference between subsequent maxima and minima is therefore  $\pi$ .

Different echoes with different  $L$  and with different frequencies give a unique  $\Phi(B)/L$



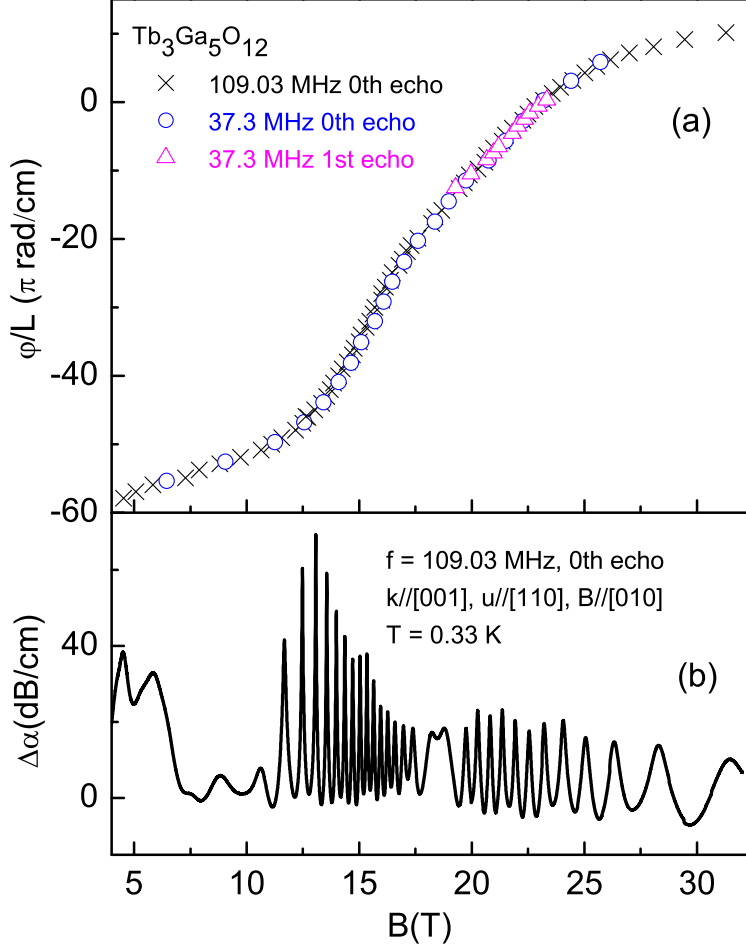


FIG. 10: (Color on line) (a) Phase  $\Phi/L$  versus magnetic field for various ultrasound signals. The frequencies and echoes are normalised to this curve using eq. 11. (b) Echo amplitude as a function of  $B$ ,  $f = 109$  MHz,  $T = 0.33$  K.

plot, normalised to one frequency  $\omega = 2\pi f$  and one length  $L$ , also shown in Fig. 10a.

We notice that the linear frequency dependence of eq. 11 and the dependence on the travel distance  $L = L_0(2n + 1)$  ( $n$  is the echo number) is strictly observed. With eq. 11 one could in principle calculate the  $\Phi(B)/L$  by using the measured velocity curves  $v_{100}(B)$  and  $v_{010}(B)$ . As pointed out above the mode  $v_{100}$  was not measured, but the Faraday mode should give the same  $B$ -dependence for symmetric strains. The  $v(B)$  curves should be measured at the same temperature, however. In addition both  $v(B)$  curves exhibit similar forms and have minima at 11 T and 20 T respectively. This leads to extremely sensitive  $\phi(B)$  dependence. Therefore only qualitative fits are possible. They give the right order of

magnitude however.

This  $\Phi(B)$ -behaviour has to be compared with another experiment performed in  $\text{CeAl}_2$  [12, 20]. Here the two velocity modes have opposite field dependencies and the agreement of the measured  $\Phi/L$  curve with eq. 11 is perfect.

## VII. CONCLUSION

Tb-Ga-Garnet with its many unusual properties has been investigated with ultrasound as a function of temperature, down to 0.3 K and at high magnetic fields. The local  $D_2$  symmetry of the six inequivalent  $\text{Tb}^{3+}$  ions leads to pronounced crystal-field effects in magnetization [9], ESR [6], and elastic constants investigated in this work. For the magneto-elastic interaction and the resulting phonon effects it was important to transform the CEF Hamiltonian to the laboratory system, where the elastic constants and the magneto-elastic Hamiltonian can be described in the usual cubic symmetry.

The temperature dependence of the elastic constants can be described quantitatively, where the important  $c_{44}$  mode is especially well fitted. The magnetic field dependence of the  $c_{44}$  mode provided crucial tests for the CEF scheme. We found very good agreement for the Faraday geometry with a minimum at 21 T and a small discrepancy for the Cotton-Mouton geometry with a minimum experimentally at 11 T and by CEF calculation at 13 T. Besides the acoustical Faraday effect [5] we showed analogous amplitude modulations for the acoustical Cotton-Mouton effect. The frequency dependence (linear in  $\omega$ ) is observed.

This detailed theoretical and experimental investigation gives a foundation for a realistic treatment of other effects, such as the phonon Hall effect [2, 3] and higher order magneto-elastic effects.

## VIII. ACKNOWLEDGMENT

We acknowledge the support of the HFML-RU/FOM and HLD at HZDR, members of the European Magnetic Field Laboratory (EMFL). This work was partly supported by the EuroMagNET II Project financed by the European Community under Contract 228043. We thank support by the Strategic Young Researcher Overseas Visits Program for Accelerating Brain Circulation from the Japan Society for the Promotion of Science (JSPS). We thank Peter Wyder for helpful discussions.

## IX. APPENDIX

### A. Summary of crystal field parameters, Coordinate systems and Tensor Operators

In the following table we list the crystal field parameters  $a_{ij}$  of TGG in  $\text{cm}^{-1}$  as found in [9].

$a_{20}$	$a_{22}$	$a_{40}$	$a_{42}$	$a_{44}$	$a_{60}$	$a_{62}$	$a_{64}$	$a_{66}$
-81.0	169.0	-2163.0	249.0	945.0	677.0	-155.0	1045.0	-4.0

(12)

The connections to the  $b_{ij}$  used in eq. 1 is given by

$$\begin{aligned}
 b_{2j} &= \frac{a_{2j}\alpha_J}{f_{2j}} & j = 0, 2 \\
 b_{4j} &= \frac{a_{4j}\beta_J}{f_{4j}} & j = 0, 2, 4 \\
 b_{6j} &= \frac{a_{6j}\gamma_J}{f_{6j}} & j = 0, 2, 4, 6
 \end{aligned}
 \tag{13}$$

with

$$\alpha_J = \frac{-1}{99} \tag{14}$$

$$\beta_J = \frac{2}{16335} \tag{15}$$

$$\gamma_J = \frac{-1}{891891} \tag{16}$$

and the  $f_{ij}$  given in eq.17.

$f_{20}$	2	$f_{21}$	$1/\sqrt{6}$
$f_{22}$	$2/\sqrt{6}$	$f_{41}$	$2/\sqrt{5}$
$f_{40}$	8	$f_{43}$	$2/\sqrt{35}$
$f_{42}$	$8/\sqrt{40}$	$f_{61}$	$\sqrt{32/21}$
$f_{44}$	$8/\sqrt{70}$	$f_{63}$	$8/\sqrt{105}$
$f_{60}$	16	$f_{65}$	$8/\sqrt{693}$
$f_{62}$	$16/\sqrt{105}$		
$f_{64}$	$16/\sqrt{126}$		
$f_{66}$	$16/\sqrt{231}$		

(17)

The notation for the tensor operators in the literature is far from being unique. We follow the notation of M.T. Hutchings [10] and P.A. Lindgård, O. Danielsen [17], but for reasons of clarity we also list the explicit form of the tensor operators  $\mathcal{O}_{l\pm m}$  used in our work in eq. 18, 19, 20. Note that the  $\mathcal{O}_{l\pm m} = \tilde{\mathcal{O}}_{l\pm m} f_{lm}$ , where  $\tilde{\mathcal{O}}_{l\pm m}$  with  $m = 0, 1 \dots l$  are the Racah operator equivalents given in Table 1 of [17]. In the following  $\{A, B\}$  denotes the anticommutator,  $J_i$  with  $i = x, y, z$  the components of the angular momentum,  $J$  the total angular momentum and  $J_{\pm} = J_x \pm iJ_y$ .

$\mathcal{O}_{2,0}$	$3J_z^2 - J(J+1)$
$\mathcal{O}_{2,+1}$	$-\frac{1}{4}\{J_+, J_z\}$
$\mathcal{O}_{2,-1}$	$\frac{1}{4}\{J_-, J_z\}$
$\mathcal{O}_{2,+2}$	$\frac{1}{2}J_+^2$
$\mathcal{O}_{2,-2}$	$\frac{1}{2}J_-^2$

(18)

$\mathcal{O}_{4,0}$	$35J_z^4 - 30J_z^2J(J+1) + 25J_z^2 - 6J(J+1) + 3J^2(J+1)^2$	(19)
$\mathcal{O}_{4,+1}$	$-\frac{1}{4}\{7J_z^3 - (3J(J+1) + 1)J_z, J_+\}$	
$\mathcal{O}_{4,-1}$	$\frac{1}{4}\{7J_z^3 - (3J(J+1) + 1)J_z, J_-\}$	
$\mathcal{O}_{4,+2}$	$\frac{1}{4}\{7J_z^2 - J(J+1) - 5, J_+^2\}$	
$\mathcal{O}_{4,-2}$	$\frac{1}{4}\{7J_z^2 - J(J+1) - 5, J_-^2\}$	
$\mathcal{O}_{4,+3}$	$-\frac{1}{4}\{J_+^3, J_z\}$	
$\mathcal{O}_{4,-3}$	$\frac{1}{4}\{J_-^3, J_z\}$	
$\mathcal{O}_{4,+4}$	$\frac{1}{2}J_+^4$	
$\mathcal{O}_{4,-4}$	$\frac{1}{2}J_-^4$	

$\mathcal{O}_{6,0}$	$231J_z^6 - 315J_z^4J(J+1) + 735J_z^4 + 105J_z^2J^2(J+1)^2 - 525J_z^2J(J+1) + 294J_z^2 - 5J^3(J+1)^3 + 40J^2(J+1)^2 - 60J(J+1)$	(20)
$\mathcal{O}_{6,+1}$	$-\frac{1}{4}\{33J_z^5 - (30J(J+1) - 15)J_z^3 + (5J^2(J+1)^2 - 10J(J+1) + 12)J_z, J_+\}$	
$\mathcal{O}_{6,-1}$	$\frac{1}{4}\{33J_z^5 - (30J(J+1) - 15)J_z^3 + (5J^2(J+1)^2 - 10J(J+1) + 12)J_z, J_-\}$	
$\mathcal{O}_{6,+2}$	$\frac{1}{4}\{33J_z^4 - (18J(J+1) + 123)J_z^2 + J^2(J+1)^2 + 10J(J+1) + 102, J_+^2\}$	
$\mathcal{O}_{6,-2}$	$\frac{1}{4}\{33J_z^4 - (18J(J+1) + 123)J_z^2 + J^2(J+1)^2 + 10J(J+1) + 102, J_-^2\}$	
$\mathcal{O}_{6,+3}$	$-\frac{1}{4}\{11J_z^3 - 3J(J+1)J_z - 59J_z, J_+^3\}$	
$\mathcal{O}_{6,-3}$	$\frac{1}{4}\{11J_z^3 - 3J(J+1)J_z - 59J_z, J_-^3\}$	
$\mathcal{O}_{6,+4}$	$\frac{1}{4}\{11J_z^2 - J(J+1) - 38, J_+^4\}$	
$\mathcal{O}_{6,-4}$	$\frac{1}{4}\{11J_z^2 - J(J+1) - 38, J_-^4\}$	
$\mathcal{O}_{6,+5}$	$-\frac{1}{4}(J_+^5J_z + J_zJ_+^5)$	
$\mathcal{O}_{6,-5}$	$\frac{1}{4}(J_-^5J_z + J_zJ_-^5)$	
$\mathcal{O}_{6,+6}$	$\frac{1}{2}J_+^6$	
$\mathcal{O}_{6,-6}$	$\frac{1}{2}J_-^6$	

For  $l = 6, m = 6, 4, 2$  for  $l = 4, m = 4, 2$  and for  $l = 2, m = 2$  we also employ the notation  $\mathcal{O}_{lm} = \mathcal{O}_{l+m} + \mathcal{O}_{l-m}$  which is redundant of course, but since it is widely used, in particular in [9] we nonetheless adopt it in eq. 1 and whenever there is no need to introduce  $\mathcal{O}_{l+m}$  and  $\mathcal{O}_{l-m}$  separately. As it is common we also introduce the operators  $\mathcal{O}_{xy}, \mathcal{O}_{xz}$  and  $\mathcal{O}_{yz}$  defined as the anticommutator  $\mathcal{O}_{ij} = \frac{1}{2}\{J_i, J_j\}$  with  $i, j = x, y, z$  of the angular momentum operators  $J_x, J_y, J_z$ .

Next we list the transformations from the local systems  $l_i, i = 1, \dots, 6$  to the laboratory system. The first column gives the transformation matrices, column 2,3,4 give the unit

vectors in the local systems and the last three columns give the Euler angles in the notation of [14].

<i>Matrix</i>	$(e_x)_{local}$	$(e_y)_{local}$	$(e_z)_{local}$	$\alpha$	$\beta$	$\gamma$
$R^1 = \begin{pmatrix} 0 & \frac{1}{\sqrt{2}} & \frac{1}{\sqrt{2}} \\ 0 & -\frac{1}{\sqrt{2}} & \frac{1}{\sqrt{2}} \\ 1 & 0 & 0 \end{pmatrix}$	$[001]_c$	$[\bar{1}\bar{1}0]_c$	$[110]_c$	$\alpha_1 = 0$	$\beta_1 = \frac{\pi}{2}$	$\gamma_1 = \frac{3\pi}{4}$
$R^2 = \begin{pmatrix} 0 & -\frac{1}{\sqrt{2}} & \frac{1}{\sqrt{2}} \\ 1 & 0 & 0 \\ 0 & \frac{1}{\sqrt{2}} & \frac{1}{\sqrt{2}} \end{pmatrix}$	$[010]_c$	$[\bar{1}01]_c$	$[101]_c$	$\alpha_2 = \frac{\pi}{2}$	$\beta_2 = \frac{\pi}{4}$	$\gamma_2 = \pi$
$R^3 = \begin{pmatrix} 1 & 0 & 0 \\ 0 & \frac{1}{\sqrt{2}} & \frac{1}{\sqrt{2}} \\ 0 & -\frac{1}{\sqrt{2}} & \frac{1}{\sqrt{2}} \end{pmatrix}$	$[100]_c$	$[01\bar{1}]_c$	$[011]_c$	$\alpha_3 = \frac{3\pi}{2}$	$\beta_3 = \frac{\pi}{4}$	$\gamma_3 = \frac{\pi}{2}$
$R^4 = \begin{pmatrix} 0 & \frac{1}{\sqrt{2}} & -\frac{1}{\sqrt{2}} \\ 0 & \frac{1}{\sqrt{2}} & \frac{1}{\sqrt{2}} \\ 1 & 0 & 0 \end{pmatrix}$	$[001]_c$	$[110]_c$	$[\bar{1}\bar{1}0]_c$	$\alpha_4 = 0$	$\beta_4 = \frac{\pi}{2}$	$\gamma_4 = \frac{\pi}{4}$
$R^5 = \begin{pmatrix} 0 & \frac{1}{\sqrt{2}} & \frac{1}{\sqrt{2}} \\ 1 & 0 & 0 \\ 0 & \frac{1}{\sqrt{2}} & -\frac{1}{\sqrt{2}} \end{pmatrix}$	$[010]_c$	$[101]_c$	$[10\bar{1}]_c$	$\alpha_5 = \frac{\pi}{2}$	$\beta_5 = \frac{3\pi}{4}$	$\gamma_5 = \pi$
$R^6 = \begin{pmatrix} 1 & 0 & 0 \\ 0 & \frac{1}{\sqrt{2}} & -\frac{1}{\sqrt{2}} \\ 0 & \frac{1}{\sqrt{2}} & \frac{1}{\sqrt{2}} \end{pmatrix}$	$[100]_c$	$[011]_c$	$[0\bar{1}1]_c$	$\alpha_6 = \frac{\pi}{2}$	$\beta_6 = \frac{\pi}{4}$	$\gamma_6 = \frac{3\pi}{2}$

(21)

Using the appropriate representations of the rotation operators  $D(\alpha, \beta, \gamma) = \exp(i\gamma J_z) \exp(i\beta J_y) \exp(i\alpha J_x)$  for angular momenta  $j=2,4,6$  as given e.g. in eq.(4.1.12) of ref.[14] the rotated Hamiltonians  $\mathcal{H}^{l_i}$  take the form

$$\begin{aligned}
\mathcal{H}^{l_i} = & b_{20}^{l_i} \mathcal{O}_{20} + b_{2,-1}^{l_i} \mathcal{O}_{2,-1} + b_{2,+1}^{l_i} \mathcal{O}_{2,+1} + b_{2,+2}^{l_i} \mathcal{O}_{2,+2} + b_{2,-2}^{l_i} \mathcal{O}_{2,-2} + b_{40}^{l_i} \mathcal{O}_{40} + b_{4,-1}^{l_i} \mathcal{O}_{4,-1} \\
& + b_{4,+1}^{l_i} \mathcal{O}_{4,+1} + b_{4,-2}^{l_i} \mathcal{O}_{4,-2} + b_{4,+2}^{l_i} \mathcal{O}_{4,+2} + b_{4,-3}^{l_i} \mathcal{O}_{4,-3} + b_{4,+3}^{l_i} \mathcal{O}_{4,+3} + b_{44}^{l_i} \mathcal{O}_{44} + b_{60}^{l_i} \mathcal{O}_{60} \\
& + b_{6,-1}^{l_i} \mathcal{O}_{6,-1} + b_{6,+1}^{l_i} \mathcal{O}_{6,+1} + b_{6,-2}^{l_i} \mathcal{O}_{6,-2} + b_{6,+2}^{l_i} \mathcal{O}_{6,+2} + b_{6,-3}^{l_i} \mathcal{O}_{6,-3} + b_{6,+3}^{l_i} \mathcal{O}_{6,+3} + b_{64}^{l_i} \mathcal{O}_{64} \\
& + b_{6,-5}^{l_i} \mathcal{O}_{6,-5} + b_{6,+5}^{l_i} \mathcal{O}_{6,+5} + b_{6,-6}^{l_i} \mathcal{O}_{6,-6} + b_{6,+6}^{l_i} \mathcal{O}_{6,+6}.
\end{aligned}
\tag{22}$$

The complex coefficients  $b_{l_i \pm m}^{l_i}$  are then linear combinations of the original coefficients  $a_{ij}$ .

As an example we list the resulting Hamiltonian obtained by rotating eq.1 from  $l_1$  to the laboratory system in eq.23. All  $b_{l_{\pm m}}^{l_1}$ , which are not listed in eq.23 vanish for this rotation from  $l_1$  to the laboratory system, also for this rotation no coefficients with odd  $j$  occur.

$b_{2,+2}^{l_1}$	$\frac{-i}{4}(\sqrt{6}a_{20} + 2a_{22})\frac{\alpha_J}{f_{22}}$	(23)
$b_{2,0}^{l_1}$	$\frac{1}{2}(-a_{20} + \sqrt{6}a_{22})\frac{\alpha_J}{f_{20}}$	
$b_{2,-2}^{l_1}$	$\frac{i}{4}(\sqrt{6}a_{20} + 2a_{22})\frac{\alpha_J}{f_{22}}$	
$b_{4,+4}^{l_1}$	$\frac{1}{16}(-\sqrt{70}a_{40} - 2(2\sqrt{7}a_{42} + a_{44}))\frac{\beta_J}{f_{44}}$	
$b_{4,+2}^{l_1}$	$\frac{i}{8}(\sqrt{10}a_{40} - 4a_{42} - 2\sqrt{7}a_{44})\frac{\beta_J}{f_{42}}$	
$b_{4,+0}^{l_1}$	$\frac{1}{8}(3a_{40} - 2\sqrt{10}a_{42} + \sqrt{70}a_{44})\frac{\beta_J}{f_{40}}$	
$b_{4,-2}^{l_1}$	$\frac{-i}{8}(\sqrt{10}a_{40} - 4a_{42} - 2\sqrt{7}a_{44})\frac{\beta_J}{f_{42}}$	
$b_{4,-4}^{l_1}$	$\frac{1}{16}(-\sqrt{70}a_{40} - 2(2\sqrt{7}a_{42} + a_{44}))\frac{\beta_J}{f_{44}}$	
$b_{6,+6}^{l_1}$	$\frac{i}{32}(\sqrt{231}a_{60} + 3\sqrt{55}a_{62} + \sqrt{66})a_{64} + a_{66})\frac{\gamma_J}{f_{66}}$	
$b_{6,+4}^{l_1}$	$\frac{1}{32}(3\sqrt{14}a_{60} - \sqrt{30}a_{62} - 26a_{64} - \sqrt{66}a_{66})\frac{\gamma_J}{f_{64}}$	
$b_{6,+2}^{l_1}$	$\frac{-i}{32}(\sqrt{105}a_{60} - 17a_{62} + \sqrt{30}a_{64} + 3\sqrt{55}a_{66})\frac{\gamma_J}{f_{62}}$	
$b_{6,0}^{l_1}$	$\frac{1}{16}(-5a_{60} + \sqrt{105}a_{62} - 3\sqrt{14}a_{64} + \sqrt{231}a_{66})\frac{\gamma_J}{f_{60}}$	
$b_{6,-2}^{l_1}$	$\frac{i}{32}(\sqrt{105}a_{60} - 17a_{62} + \sqrt{30}a_{64} + 3\sqrt{55}a_{66})\frac{\gamma_J}{f_{62}}$	
$b_{6,-4}^{l_1}$	$\frac{1}{32}(3\sqrt{14}a_{60} - \sqrt{30}a_{62} - 26a_{64} - \sqrt{66}a_{66})\frac{\gamma_J}{f_{64}}$	
$b_{6,-6}^{l_1}$	$\frac{-i}{32}(\sqrt{231}a_{60} + 3\sqrt{55}a_{62} + \sqrt{66}a_{64} + a_{66})\frac{\gamma_J}{f_{66}}$	

- [1] G. Winkler, Magnetic Garnets, Vieweg, Braunschweig (1981).
- [2] C. Strohm et al., Phys. Rev. Lett. **96**, 155901 (2005).
- [3] A.V. Inyushin and A.N. Taldenkov, JETP Letters **86**, 379 (2007)
- [4] A.Sytcheva, U. Löw, S. Yasin, J. Wosnitza, S. Zherlitsyn, T. Goto, P. Wyder, and B.Lüthi, J. Low Temp. Phys. **159**, 126 (2010).
- [5] A. Sytcheva, U. Löw, S. Yasin, J. Wosnitza, S. Zherlitsyn, P. Thalmeier, T. Goto, P. Wyder, and B. Lüthi Phys. Rev. B **81**, 214415 (2010).
- [6] U. Löw, S. Zvyagin, M. Ozerov, U. Schaufuss, V. Kataev, B. Wolf, and B. Lüthi, Eur. Phys. J. B.(2013) 86:87.
- [7] K. Kamazawa et al., Phys. Rev. B **78**, 064412 (2008).
- [8] K. Araki et al., Eur. Phys. J. B **61**, 257 (2008).

- [9] M.Guillot et al., J.Phys. C **18**, 3547 (1985).
- [10] M. T. Hutchings, Solid State Phys. **16**, 227-273 (1964).
- [11] B. G. Wybourne, Spectroscopic Properties of Rare Earths (J. Wiley and Sons, Inc., New York, 1965).
- [12] B. Lüthi, Physical Acoustics in the Solid State (Springer,2005), 2nd edn. 2007.
- [13] R.Z. Levitin, et. al.Physics of the Solid State, Vol. 44, No. 11,(2107-2111)2002.
- [14] A.R. Edmonds, Angular Momentum in Quantum Mechanics, Princeton Landmarks in Physics, (Princeton University Press 1974).
- [15] J. Hammann and P. Manneville, J. de Phys. **34**, 615 (1973).
- [16] Y.P. Varshny, Phys. Rev. B **2**, 3952 (1970).
- [17] P.A. Lindgård, O. Danielsen J. Phys. C **7**, 1523 (1974).
- [18] B.E.Keen,D.P.Landau, W.P. Wolf, Phys.Lett. **23**,(1966) 202. (ver)
- [19] A.V. Inyushin and A.N. Taldenkov, JETP Letters **111**, 760 (2010).
- [20] B.Lüthi, C.Lingner, Z. Phys. **34**, 157 (1979).